



Force field comparison for molecular dynamics simulations of liquid membranes

Oleg V. Kashurin^{a,b,*}, Nikolay D. Kondratyuk^{a,b,c}, Alexander V. Lankin^{a,b}, Genri E. Norman^{a,b,c}

^a Moscow Institute of Physics and Technology (National Research University), Institutskiy Pereulok 9, Dolgoprudny, 141701, Moscow oblast, Russia

^b Joint Institute for High Temperatures, Russian Academy of Sciences, Izhorskaya 13 Bldg 2, Moscow, 125412, Russia

^c HSE University, Myasnitskaya 20, Moscow, 101000, Russia

ARTICLE INFO

Keywords:

Diisopropyl ether
Molecular dynamics
Force field
Shear viscosity
Solubility
Interfacial tension

ABSTRACT

To accelerate the development of liquid ion-selective barriers based on ethers, we compare the all-atom force fields GAFF, OPLS-AA with charge correction 1.14*CM1A (OPLS-AA/CM1A), CHARMM version 36 (CHARMM36), and COMPASS for diisopropyl ether (DIPE) to determine the most appropriate model for further simulations of liquid membranes. Utilizing the selected force fields, we calculate the density and shear viscosity of DIPE across a temperature range of 243–333 K. Furthermore, we use CHARMM36 with mTIP3P water model and COMPASS with its own water model to evaluate the mutual solubility and interfacial tension between DIPE and water, estimate the partition coefficients of ethanol in DIPE + Ethanol + Water systems. Based on our comparative study, we conclude that CHARMM36 is the most suitable force field for modeling ether-based liquid membranes.

1. Introduction

Ethers, crown ethers, and cryptands are regarded as highly promising components for liquid ion-selective barriers [1–3]. These barriers form a liquid membrane, comprising an ether layer sandwiched between two aqueous solution layers. The selective permeability of this layer to various ions presents opportunities for isolating rare elements such as lithium or rubidium from aqueous solutions. Additionally, it holds potential for developing innovative electrochemical power sources, including redox flow batteries [4–7].

Owing to the vast array of parameters and properties associated with liquid membranes, their experimental study is quite complicated [8–10]. Because of the complexity of such systems, molecular dynamics (MD) methods can be helpful. MD methods are commonly used for studying the structures and properties of liquids [11–15]. Several examples of dynamic property calculations for aqueous solutions can be found in the literature [16–19].

To apply MD methods for studying the properties of composite systems, it is crucial to ensure that the chosen MD model accurately reproduces the physical properties relevant to the considered processes. When estimating the ion selectivity of an ether layer, it is essential to accurately reproduce the mobility and transport properties of the ether

itself [20–23]. Practically, this necessitates that the force field accurately reproduces diffusion and shear viscosity.

It is also necessary to accurately describe thermodynamic properties, such as pVT properties [22,24]. Besides that, the free energy of solvation is very important when modeling solutions. Free energy of solvation is closely linked to solubility and partition coefficients. These properties are important because the model should reproduce the distribution of ions in the aqueous and ether phases, as well as the mutual solubility of ether and water. Interfacial tension also plays an important role in membrane systems as it controls the permeability of the layers and stability of the membrane itself [24].

To assess the accuracy of an MD model, it is necessary to compare simulation results with experimental data. Therefore, it is convenient to model substances for which experimental data on the desired properties already exist. Experimental data on the transport and thermodynamic properties of crown ethers and cryptands are extremely limited. Diisopropyl ether (DIPE) stands out in this regard. It is a secondary ether with the formula $C_6H_{14}O$, known for its good selectivity towards lithium ions [1]. A considerable amount of experimental data on its physical properties is available in the literature [25–32].

Three experimental works are of particular significance to us. The study by Meng et al. [25] thoroughly investigates the temperature de-

* Corresponding author at: Joint Institute for High Temperatures, Russian Academy of Sciences, Izhorskaya 13 Bldg 2, Moscow, 125412, Russia.
E-mail address: oleg.kashurin20@gmail.com (O.V. Kashurin).

pendency of DIPE density and shear viscosity. The work by Cardenas et al. [32] provides experimental data on interfacial tension between DIPE and water. The work by Arce et al. [30] contains the experimental data on the composition of the aqueous and organic phases of DIPE + Ethanol + Water systems. It makes DIPE a convenient subject for testing the force fields, which can be applied to a broader range of ethers, including crown ethers and cryptands.

Interatomic potentials, more commonly referred to as force fields, are the physical basis of MD methods. They are mathematical functions used to calculate the potential energy of a system of atoms with given spatial positions. The modeling accuracy of MD depends on how precisely the force field reproduces interactions between atoms and molecules. Validating a wide variety of force fields based on experimental or quantum chemical data is an important task in modern MD research [33–38].

For the diisopropyl ether, there are several MD simulation works [5, 39,40]. In the work [5], MD method is used to study the structure of an electrolyte containing polysulfides and DIPE as a co-solvent. The OPLS-AA force field [41] is used. The work also includes an experimental study of the electrolyte structure. The simulation results closely match the experimental data. The paper [39] presents the ComBat database for the design of electrolytes for lithium-sulfur batteries. The authors calculate a set of physical parameters for a large number of solutions, such as conductivity and viscosity of electrolytes containing DIPE as a co-solvent. The OPLS-AA force field [42] is used for solvents. The work [40] investigates the influence of the DIPE solvent on the synthesis of peroxyacid. MD method with the CHARMM force field is used to calculate the binding free energy.

However, the mentioned works did not study the physical properties important for ion transport through the membrane. In addition, the two studies did not have comparison of MD results with experimental data. Thus, it is still necessary to conduct a more comprehensive study using multiple force fields and make comparisons on both the thermodynamic and transport properties of DIPE and its solution with water.

This work is devoted to the comparison of common force fields in terms of their ability to reproduce the transport and thermodynamic properties of ethers and ether + water systems. We perform calculations using four common all-atom force fields: GAFF [43], OPLS-AA/CM1A (OPLS-AA [41] with charge correction 1.14*CM1A [44,42]), CHARMM36 (CHARMM version 36 [45,46]), and COMPASS [47]. We calculate the density and shear viscosity of DIPE over a wide temperature range using the selected force fields. We also estimate the mutual solubility of DIPE and water, calculate interfacial tension between DIPE and water, and evaluate the partition coefficients of ethanol in DIPE + Ethanol + Water systems. Based on the obtained results, we choose the most suitable force field for modeling ether-based liquid membranes. This will allow the use of MD methods for modeling the transport of alkali metal ions through the contact of water and ether, as well as studying the distribution of these ions over the aqueous and organic phases in liquid ion-selective barriers based on ethers.

The article is organized as follows. We give general information about modeling techniques and methods in Section 2, which includes the brief description and comparison of the used force fields and MD simulation details. In Section 3, we provide the main results of the paper: the DIPE equilibrium density and shear viscosity calculations, as well as the estimations of mutual solubility of DIPE and water, the interfacial tension between DIPE and water, the ethanol partition coefficients in DIPE + Ethanol + Water systems. Section 4 contains the discussion of the results.

2. Modeling technique

2.1. Force fields

A large number of different force fields are used in MD simulations to model the properties of liquids. The most common force fields for

modeling small molecules are AMBER, MMFF, GAFF, Gromos, OPLS-AA, TraPPE, CHARMM, ReaxFF, COMPASS, etc. Force fields like GAFF, OPLS-AA, CHARMM are parameterized for a large number of organic molecules. This makes them convenient for modeling complex systems containing multi-component mixtures, such as those arising when simulating ion transport through ion-selective liquid membranes. This property largely determined our choice of GAFF, OPLS-AA, and CHARMM force fields for comparison.

We also include the COMPASS force field in our comparison. GAFF, OPLS-AA, and CHARMM are class I force fields, which treat the intramolecular energy via diagonal quadratic terms, whereas COMPASS is a class II force field. In this family of force fields [48], the non-diagonal elements of intramolecular energy are included such as bond-bond, bond-angle, etc. Such force fields have a much more complex functional form and demonstrate good accuracy in many problems [49,50]. However, the COMPASS force field is proprietary, which limits the possibility of its use in further modeling of multi-component systems with ions.

GAFF force field is developed for rational drug design [43]. Optimization of GAFF parameters is performed for approximately 2000 molecules, most of which are small, simple molecules widely used in force field development. Van der Waals (vdW) parameters are taken from AMBER, where they are obtained using *ab initio* and empirical methods, optimizing the density and enthalpy of vaporization. Partial charges are obtained using *ab initio* calculations. Bond parameters are derived from X-ray spectroscopy, *ab initio* calculations, and Parmscan. Angles and torsions are calculated using *ab initio* methods and Parmscan.

OPLS-AA force field is developed for modeling organic molecules and peptides [41]. Its parameterization, akin to GAFF, relies on extensive optimization across a wide array of organic molecules. vdW parameters are determined empirically, with some borrowed from the preceding version, OPLS-UA. Charges are empirically derived, using approximations to capture the characteristics of organic liquids accurately. Bond and angle parameters are adopted from AMBER and, to some extent, from CHARMM. The torsional terms are parameterized through *ab initio* methods.

CHARMM version 36 is a highly modified 27th version of this force field [45]. CHARMM version 27 includes parameters for proteins, nucleic acids, lipids, and carbohydrates. The main changes in version 36 are aimed at improving the quality of lipid modeling. In this force field, the charges, vdW, and torsion parameters are updated using *ab initio* methods. The bond and angle parameters are retained from the previous version, where they are obtained by combining *ab initio* and empirical approaches. CHARMM force field consists of various parameterizations for different chemical groups of molecules [51–53]. For molecules not falling in any of the groups an extension of the CHARMM force field – CHARMM General Force Field [54] – is used.

The COMPASS force field is based on the PCFF force field [47]. A hybrid approach, incorporating both *ab initio* and empirical methods, is utilized to parameterize COMPASS. In addition to the molecular classes covered by the PCFF force field, a number of new classes have been parameterized. Non-bonded parameters have been completely reparameterized. Some of the bonded parameters were taken from PCFF, while those for the missing functional groups were parameterized from scratch.

All the force fields take into account valent and non-valent interactions between atoms:

$$E_{total} = E_{bond} + E_{angle} + E_{dihedral} + E_{non-valent}.$$

In OPLS-AA and GAFF, the valent interactions are described by harmonic vibrations of covalent bonds b , angles between three atoms θ and dihedral interactions ϕ :

$$E_{bond} = \sum_b k_b (b - b_0)^2, E_{angle} = \sum_a k_a (\theta - \theta_0)^2,$$

$$E_{dihedral} = \sum_d \sum_n \frac{k_{d,n}}{2} [1 + \cos(n\phi - \gamma)].$$

In the CHARMM case, the valent interactions contain more terms – improper and Uray-Bradley interactions:

$$E_{improper} = \sum_{improvers} k_{\omega} (\omega - \omega_0)^2, \quad E_{U-B} = \sum_{U-B} k_u (u - u_0)^2.$$

E_{bond} , E_{angle} , and $E_{dihedral}$ have the same functional form as for the GAFF force field. Term E_{U-B} is called the Uray-Bradley sum. The summation in the term occurs over all chains of 3 successively connected atoms. The term $E_{improper}$ describes the energy of out-of-plane atoms bending, and the summation is performed over a set of 4 atoms that are not connected in series.

For GAFF, OPLS-AA, and CHARMM force fields, non-bonded interactions of atoms are described by Lennard-Jones and electrostatic potentials:

$$E_{non-valent} = \sum_{non-valent} \left(4\epsilon_{ij} \left[\left(\frac{\sigma_{ij}}{r_{ij}} \right)^{12} - \left(\frac{\sigma_{ij}}{r_{ij}} \right)^6 \right] + \frac{q_i q_j}{\epsilon_r r_{ij}} \right)$$

Different combination rules are used to determine interatomic Lennard-Jones parameters ϵ_{ij} and σ_{ij} for atoms of different types as suggested in original papers. The Lorentz-Berthelot combination rule is used for GAFF [43] and CHARMM36 [45], and the geometric mean combination rule is used for OPLS-AA/CM1A [41].

1-4 intramolecular interactions are also scaled differently. In GAFF, scale factors are 1/2 and 1/1.2 for vdW and electrostatic interactions, respectively. In OPLS-AA/CM1A, the scale factor is 1/2 for both vdW and electrostatic interactions. In CHARMM36, the electrostatic interaction is not scaled, and vdW weight is determined based on a special set of parameters.

The functional form of the COMPASS force field is the most complex among the considered force fields. The bonded and angle interactions are treated as non-harmonic oscillators. Also, it takes into account non-diagonal energy cross-terms. The total energy of liquid is described as:

$$E_{total} = E_b + E_{\theta} + E_{\phi} + E_{\chi} + E_{b,b'} + E_{b,\theta} + E_{b,\phi} + \\ + E_{\theta,\phi} + E_{\theta,\theta'} + E_{\theta,\theta',\phi} + E_q + E_{vdW},$$

where for example

$$E_b = \sum_b \left[k_2 (b - b_0)^2 + k_3 (b - b_0)^3 + k_4 (b - b_0)^4 \right],$$

$$E_{b,\theta} = \sum_{b,\theta} \left[M (b - b_0) (\theta - \theta_0) \right].$$

The cross-terms $E_{b,\phi}$, $E_{\theta,\phi}$, $E_{\theta,\theta'}$, $E_{\theta,\theta',\phi}$ are determined analogically. The non-valent interactions are presented as:

$$E_q = \sum_{ij} \frac{q_i q_j}{\epsilon_r r_{ij}}, \quad E_{vdW} = \sum_{ij} \epsilon_{ij} \left[2 \left(\frac{r_{ij}^0}{r_{ij}} \right)^9 - 3 \left(\frac{r_{ij}^0}{r_{ij}} \right)^6 \right],$$

using the Waldman-Hagler combination rule [55]

$$r_{ij}^0 = \left(\frac{(r_i^0)^6 + (r_j^0)^6}{2} \right)^{1/6}, \quad \epsilon_{ij} = 2 \sqrt{\epsilon_i \cdot \epsilon_j} \left(\frac{(r_i^0)^3 \cdot (r_j^0)^3}{(r_i^0)^6 + (r_j^0)^6} \right).$$

In COMPASS force field, 1-4 intramolecular interactions are not scaled and are fully accounted for.

The GAFF parameters are generated using the Antechamber program [56]. The calculation of partial charges on atoms is carried out according to [57], and the interactions are parameterized according to [56]. Parameters for OPLS-AA are generated on the LigParGen server [58]. For the partial charges, the correction 1.14*CM1A [44,42] is applied. Interaction parameters for CHARMM36 are generated in CHARMM-GUI [59–61]. COMPASS parametrization is generated using the *msi2lmp* tool in LAMMPS, developed by Pieter in 't Veld. All the original interaction parameters applied for the parametrization of the current molecules are provided on the LAMMPS GitHub repository [62].

We use the CHARMM-modified mTIP3P water model [63] when modeling water in CHARMM36. This model specifies a 3-site rigid water molecule with charges and Lennard-Jones parameters assigned to each of the 3 atoms. The model is derived from the standard TIP3P model by adding the Lennard-Jones interaction to hydrogen atoms [64]. This modification is introduced to prevent cases where hydrogen atoms get too close to other atoms and create singularities when calculating the Coulomb interaction. The water model for COMPASS was published as a part of the INTERFACE force field [65,66].

Thus, we use these force fields for the comparison:

- General AMBER Force Field [43] (GAFF in the text),
- Optimized Potentials for Liquid Simulations-All Atom (OPLS-AA) [41] from Jorgensen's research group with 1.14*CM1A [44,42] charge corrections (OPLS-AA/CM1A in the text),
- Chemistry at Harvard Macromolecular Mechanics ver. 36 [45, 46] with its own designed modification of three-site water model mTIP3P [63] (CHARMM36 in the text),
- COMPASS [47] with its own three-site water model [65,66] (COMPASS in the text).

2.2. Molecular dynamics simulation details

The calculations in the GAFF, OPLS-AA/CM1A, and CHARMM36 force fields are performed using the GRONINGEN Machine for Chemical Simulations (GROMACS) software package [67–69]. Large-scale Atomic/Molecular Massively Parallel Simulator (LAMMPS) [70–72] is chosen for COMPASS because all the interaction cross-terms are not fully presented in GROMACS. However, Burrows et al. [73] could implement the part of the COMPASS force field valent interactions inside GROMACS for the calculation of phase transitions in alkanes.

The integration step is set to 1 fs in all the calculations. Periodic boundary conditions are used to mitigate edge effects. The interaction cutoff is applied to vdW and Coulomb interactions. The cutoff radius is 1.2 nm for vdW interactions. For the Coulomb interaction, it is set automatically to achieve the required calculation accuracy. For GAFF, OPLS-AA/CM1A, and COMPASS, dispersion tail corrections to energy and pressure are taken into account, compensating for the potential truncation [47,74]. CHARMM36 is parameterized without accounting for the dispersion corrections, that is why we do not perform tail corrections when using CHARMM36. These corrections play an important role in the prediction of various properties, such as the surface tension and structure [75,76].

In LAMMPS, the long-range electrostatic part of the interaction is calculated using the particle-particle particle-mesh (PPPM) method [77, 78] with a specified accuracy parameter of 10^{-4} kJ/mol. In GROMACS, it is calculated by the Particle Mesh Ewald (PME) method [79].

In LAMMPS, the Nosé-Hoover thermostat and barostat are used to maintain the NVT and NPT ensembles, respectively [80–82]. In GROMACS, the C-rescale barostat [83] and the V-rescale thermostat [84] are used to maintain the NPT ensemble during relaxation, while the Nosé-Hoover thermostat is used to maintain the NVT ensemble during production runs.

Optimization for hybrid architectures [85,86] is performed to achieve high computational performance.

3. Results

3.1. Density of diisopropyl ether

For the comparison of force fields on pvT property data we calculate DIPE density using all 4 force fields. For the density calculations, we use a set of 64 different cubic unit cells containing 3375 DIPE molecules. We choose such a number of molecules because it finally provides a balance between the magnitude of fluctuations and computational complexity for the viscosity. Several different cells are needed for further

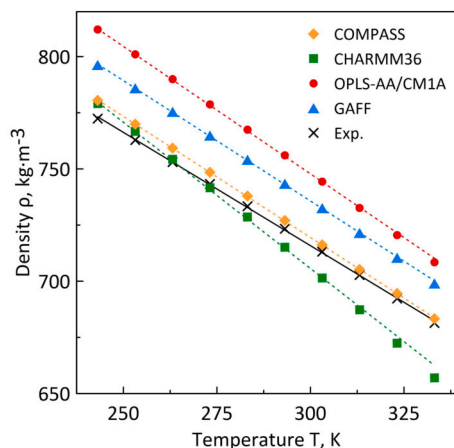


Fig. 1. DIPE density dependencies on temperature at pressure 0.1 MPa obtained for the different force fields. The crosses represent experimental values from the work [25]. Straight lines show least squares approximations of dependencies. The errors are smaller than the size of the markers.

viscosity calculations. The initial configurations are set in the form of a $15 \times 15 \times 15$ cubic lattice with a constant of 10 \AA . The molecules are oriented randomly. This configuration corresponds to the rarefied gas. To ensure uniqueness, different seeds for initial velocity generation and molecules' orientations are used for each cell. The relaxation process for each cell consists of three stages: cell compression to the experimental density, modeling in the NPT ensemble for 0.3 ns, and modeling in the NVT ensemble for 0.1 ns. The density calculations are carried out in the NPT ensemble for 0.5 ns, with density values recorded every 0.1 ps. The equilibrium density is determined as the average of 5000×64 values.

The statistical errors of density values are defined by the automated blocking method [87]. Using this method, the statistical errors are found to be about 0.01%. However, the study by the group of Hasse [88] showed that systematic errors for density in MD calculations are typically about 0.1% or even 1%. It is important to correctly estimate errors, but in our case, the difference between values for different force fields is much bigger than possible errors. That is why we can omit to calculate systematic errors for density values. A similar conclusion is valid when calculating shear viscosity of DIPE.

The DIPE density values are calculated at 0.1 MPa for temperatures ranging from 243.15 to 333.15 K using all four force fields. The obtained values are presented together with the experimental data in Fig. 1. The experimental values are taken from [25]. The uncertainty of experimental values is 0.2%.

GAFF and OPLS-AA/CM1A overestimate the density values, but the difference between the calculated values and experimental data decreases linearly with increasing temperature. OPLS-AA/CM1A yields the worst agreement between the obtained values and the experiment [25] among the considered force fields. The error reaches 5% at 243.15 K and 4% at 333.15 K. GAFF predicts density slightly better than OPLS-AA/CM1A, with the density values overestimated by 3.1–2.6% over the entire temperature range.

CHARMM36 tends to overestimate density at low temperatures and underestimate it at high temperatures. The deviation of density values from the experiment varies from 1% at 243.15 K to 3.6% at 333.15 K. It provides the best convergence among all the force fields in the region of 243.15–273.15 K, but at higher temperatures, it is outperformed by COMPASS and GAFF. The temperature dependence of density for CHARMM36 turned out to be the most nonlinear among all other force fields. Consequently, a significant density underestimation is expected at temperatures higher than 333.15 K.

COMPASS slightly overestimates the density values and provides the most accurate agreement between MD and experimental data in predicting DIPE density. The error ranges from 1.0% at 243.15 K to 0.3% at 333.15 K.

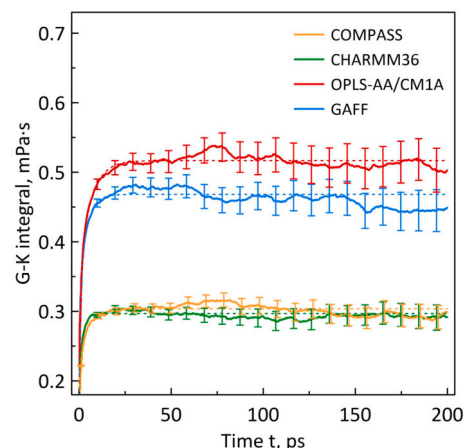


Fig. 2. Dependence of viscosity integral on upper time limit at temperature 303.15 K and pressure 0.1 MPa for all the force fields. The colors are the same as in Fig. 1. The dashed lines are the approximations of the averaged integral by the equation (4).

3.2. Shear viscosity of diisopropyl ether

The viscosity of organic liquids is a crucial property for modeling of physical processes [9,89–92]. The equilibrium approach for calculating shear viscosity is the Green-Kubo method [93,94]. Viscosity is determined by the formula

$$\eta = \frac{V}{kT} \int_0^\infty C_\sigma dt, \quad (1)$$

where V is the volume of the computational cell, k is the Boltzmann constant, T is the absolute temperature of the system, and C_σ is the auto-correlation function of the off-diagonal elements of the stress tensor:

$$C_\sigma = \langle \sigma_{\alpha\beta}(0) \sigma_{\alpha\beta}(t) \rangle \quad (2)$$

Angle brackets mean averaging over time and statistically independent configurations. The stress tensor $\sigma_{\alpha\beta}$ is calculated using the following formula

$$\sigma_{\alpha\beta} = \frac{1}{V} \left(\sum_{i=1}^N m_i v_{i,\alpha} v_{i,\beta} + \sum_{i=1}^{N'} r_{i,\alpha} f_{i,\beta} \right), \quad (3)$$

where $f_{i,\beta}$ is the β -component of the force acting on the i -th particle, N is the number of atoms in the cell, N' includes atoms from neighboring sub-domains in the case of periodic boundary conditions.

We perform MD simulations for calculating viscosity in the NVT ensemble. The same set of configurations as for calculating density is used to calculate viscosity. The unit cells of other sizes are not used because the value of shear viscosity is not influenced by size effects for systems containing about 3000 molecules [95,96].

The numerical procedure for calculating viscosity is carried out according to the time decomposition method (TDM) [97,98]. For each cell, an NVT trajectory of 1000 ps length is calculated. Thus, a set of 64 trajectories is generated for each force field. For each trajectory, the auto-correlation function is calculated and then integrated. The result is a set of 64 integrals that we call individual viscosity integrals. The averaged viscosity integral (1) is calculated as the average over the whole set of trajectories. An example of viscosity integral (1) dependency on time for a temperature of 303.15 K is shown in Fig. 2.

The calculated viscosity integral is fitted with a function of the form

$$\eta(t) = A\alpha\tau_1 \left(1 - \exp\left(-\frac{t}{\tau_1}\right) \right) + A(1-\alpha)\tau_2 \left(1 - \exp\left(-\frac{t}{\tau_2}\right) \right), \quad (4)$$

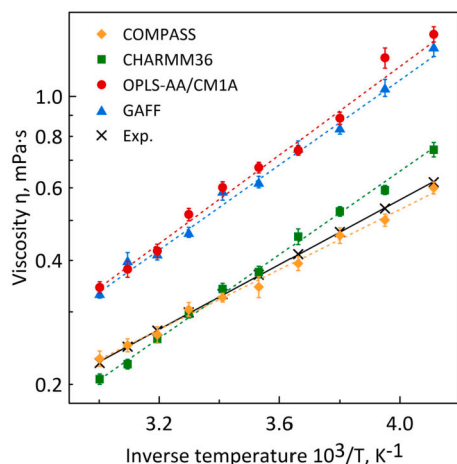


Fig. 3. Dependence of shear viscosity on the inverse temperature at 0.1 MPa for the force fields under study. The colors are the same as in Fig. 1. The crosses are plotted for the experimental data from the work [25]. Straight lines show approximations of dependencies by the Guzman-Andrade equation (6).

where A , α , τ_1 , τ_2 are fitting parameters. Thus, the viscosity is determined by the expression

$$\eta(t) = A(\alpha\tau_1 + (1 - \alpha)\tau_2). \quad (5)$$

We employ the bootstrapping method for estimating the viscosity values error [99,100]. The essence of this method is to form N bootstrap samples. The bootstrap sample is formed from a set of individual viscosity integrals. Integrals are chosen randomly, and repetitions are possible. Each bootstrap sample is the same size as the trajectory set, which is 64 in our case. For each obtained sample of integrals, the same procedure of viscosity calculation as described above is performed. The error is defined as the standard deviation of the resulting set of values. We have $N = 256$ in our calculations.

Using all the force fields, the DIPE shear viscosity is calculated for pressure of 0.1 MPa and temperatures in the range of 243.15–333.15 K. Dependencies of the obtained viscosity values on the inverse temperature in the logarithmic scale are shown in Fig. 3. We compare the results with experimental values which are taken from [25]. The uncertainty of experimental values is 2.0%.

The dependency of shear viscosity η on temperature is well described by the Guzman-Andrade equation [101]:

$$\eta = \eta_0 \exp\left(\frac{E_a}{RT}\right), \quad (6)$$

where E_a is the activation energy, R is the universal gas constant, T is the absolute temperature of the system, η_0 is the pre-exponential factor. Accordingly, the logarithmic dependence of viscosity on the inverse temperature is a linear function.

It can be observed from the obtained results that the GAFF and OPLS-AA/CM1A force fields overestimate the shear viscosity. They provide approximately equally low accuracy of convergence with the experiment [25]. The average error varies from 130% at low temperatures to 50% at high temperatures.

CHARMM36 overestimates viscosity values at low temperatures and underestimates them at high temperatures. The convergence with the experiment is better than for GAFF and OPLS-AA/CM1A. The error is 10–20% at 243.15–273.15 K and 2–9% at 283.15–333.15 K.

COMPASS provides good agreement with the experiment. In the temperature range of 243.15–283.15 K, COMPASS slightly underestimates the viscosity values, with a maximum error of 6%. The best convergence with experimental data is observed in the region of 293.15–333.15 K, where the maximum error does not exceed 2%. In this case, the ob-

tained viscosity values coincide with the experiment within the estimated error.

3.3. Mutual solubility of DIPE and water

The following method is employed to estimate solubility. It is based on forming a layer of the aqueous phase and the organic phase (where DIPE predominates) in the cell. The example of this unit cell is presented in Fig. 4a. The layers are perpendicular to the z axis. Such a cell is simulated for a certain time in the NVT ensemble to accumulate sufficient statistics to calculate the steady-state density profile along the z axis. An example of obtained density profiles is shown in Fig. 4b.

If the calculation time is sufficiently long, the dependency of water and DIPE density on the z coordinate will exhibit distinguishable horizontal sections in the areas corresponding to the established phase layers. Taking the mean of density values in these regions, we can obtain the density of DIPE in aqueous phase (ρ_{DIPE}) and the density of water in organic phase (ρ_{water}). Then, obtaining molar concentrations $c_{\text{DIPE}} = \rho_{\text{DIPE}}/M_{\text{DIPE}}$, $c_{\text{water}} = \rho_{\text{water}}/M_{\text{water}}$, we can get the solubilities of DIPE in water and water in DIPE by computing the mole fractions of DIPE and water in the phases by formulas

$$x_{\text{DIPE}} = \frac{c_{\text{DIPE}}}{c_{\text{DIPE}} + c_{\text{water}}}, \quad x_{\text{water}} = \frac{c_{\text{water}}}{c_{\text{DIPE}} + c_{\text{water}}}. \quad (7)$$

It is worth noting that this method does not provide accurate solubility values but is suitable for order-of-magnitude estimations. Since solubility exponentially depends on the free energy of solvation, a small deviation in the free energy can lead to a significant difference in its value. Therefore, a difference of one order of magnitude in solubility implies only a 6 kJ/mol difference in the free energy of solvation.

Only the CHARMM36 and COMPASS force fields are used in the calculations because they show acceptable accuracy of both the density and viscosity of DIPE. The simulations are performed at a temperature of 298.15 K and pressure of 0.1 MPa. The results are compared with experimental data [30].

To simulate the DIPE + Water system in the CHARMM36 force field, a cell containing 48,708 water molecules and 4,350 DIPE molecules is created using GROMACS. The cell structure is the same as in the case of COMPASS. Relaxation is carried out first in the NPT ensemble for 1 ns, and then in the NVT ensemble for 0.5 ns. After that, a 5 ns NVT production calculation is performed. We present an example of the equilibrated system for estimating solubility and the obtained density distribution plot in Fig. 4.

To simulate the DIPE + Water system in the COMPASS force field, a cell containing 68,600 water molecules and 6,300 DIPE molecules is created. The Moltemplate program [103] is used to generate the initial atom coordinates. The initial coordinates of the molecules are specified on a lattice. A layer of DIPE molecules is located between two layers of water molecules, with the layers situated along the z axis. Cell relaxation is carried out in the NPT ensemble for 2 ns. It is then followed by a 2 ns NVT production run during which statistics on the density distribution along the z axis are collected.

It is better to use the NPAT ensemble instead of the usual NPT for simulations of systems with a slab geometry [104,105]. We conduct test calculations where the relaxation is made in the NPAT ensemble. The obtained solubilities coincide within the calculation accuracy with the calculations with the NPT relaxation.

The mole solubilities of DIPE in water and water in DIPE are shown in Table 1. The values are given in mole fraction and presented by an order of magnitude.

When using CHARMM36, the solubility of DIPE in water is underestimated by an order of magnitude, while the solubility of water in DIPE is of the same order as the experimental value. For the COMPASS force field, the solubility of DIPE in water is underestimated by two orders of magnitude, and the solubility of water in DIPE is underestimated by one order of magnitude.

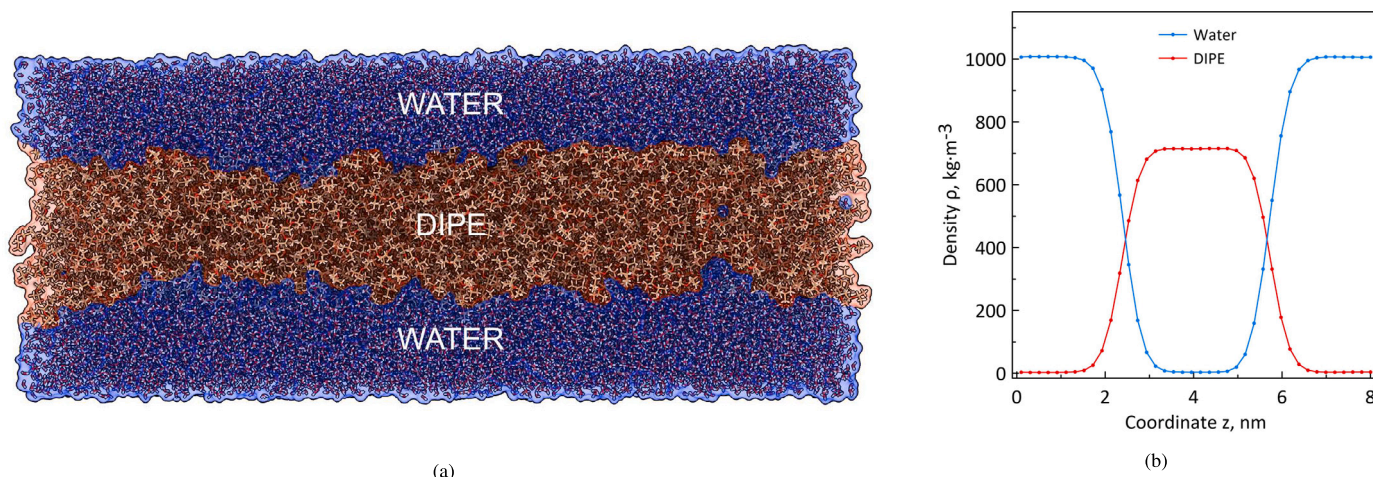


Fig. 4. (a) An example of a system for estimating solubility containing 4,350 DIPE (colored red) and 48,708 water (colored blue) molecules. The configuration is visualized in the UCSF ChimeraX [102]. (b) The example of density distribution of DIPE and water along z axis for CHARMM36 at 298.15 K and 0.1 MPa.

Table 1

Thermodynamic properties of DIPE solutions at 298.15 K and 0.1 MPa: solubility and interfacial tension, calculated in binary systems, ethanol partition coefficients, calculated in ternary systems.

Property	MD (CHARMM36)	MD (COMPASS)	Experiment
Solubility of DIPE in water, x_{DIPE} , mole fraction	$\sim 10^{-4}$	$\sim 10^{-5}$	$2.9 \cdot 10^{-2}$ [30]
Solubility of water in DIPE, x_{water} , mole fraction	$\sim 10^{-2}$	$\sim 10^{-3}$	$2.89 \cdot 10^{-2}$ [30]
Interfacial tension between DIPE and water, γ , mN/m	18.7 ± 0.8	38.0 ± 0.5	17.70 ± 0.01 [32]
Ethanol partition coefficients, k	$\sim 10^0$	$\sim 10^1$	$0.75 - 2.12$ [30]

3.4. Interfacial tension between DIPE and water

The surface tension between different substances is crucial in the liquid membrane systems, as it influences how easily ions can pass through the layers and affects the overall stability of the membrane structure. The MD methods are widely applied for such calculations for liquid-liquid interfaces [75,76,106–108].

The interfacial tension γ is calculated by the formula [109]

$$\gamma = \frac{L_z}{2} \left(\langle P_{zz} \rangle - \frac{\langle P_{xx} \rangle + \langle P_{yy} \rangle}{2} \right), \quad (8)$$

where L_z is the length of the cell in z direction and P_{xx} , P_{yy} , P_{zz} are diagonal elements of the pressure tensor.

The same cells as for calculating the mutual solubility of DIPE and water are used to calculate the interfacial tension between DIPE and water. As in the previous section, we use only CHARMM36 and COMPASS force fields.

The simulations are performed in the NVT ensemble for 2 ns. The simulated temperature is 298.15 K. The diagonal pressure tensor elements are saved every 5 fs. The errors are estimated using the automated blocking method [87].

The results are shown in Table 1. The comparison is made against the experimental data from the work [32]. The experimental error of interfacial tension values is 0.01 mN/m.

The interfacial tension for CHARMM36 force field closely matches the experimental value. The error is 6%, which is almost the same as the value's uncertainty. However, the interfacial tension for COMPASS force field is more than 2 times bigger than the experimental value.

3.5. Ethanol partition coefficients

Basically, the same method used to estimate solubility is used to estimate partition coefficients. A liquid membrane with DIPE in the middle is formed in the cell. The membrane is perpendicular to the z axis. However, in this case, the third substance, i.e. ethanol, is added to the system.

It must be distributed uniformly in the xy plane so that the entire system remains homogeneous in this plane for any value of z . An example of a system for estimating a partition coefficient is presented in Fig. 5.

The composition of both phases can be determined from density dependencies for water, DIPE, and ethanol on the z coordinate as described in part 3.3. An example of obtained density profiles is shown in Fig. 5b. Using mole ethanol fractions in organic c_1 and water c_2 phases, partition coefficient k is calculated by the formula

$$k = \frac{c_1}{c_2}. \quad (9)$$

The simulations are conducted for a temperature of 298.15 K and a pressure of 0.1 MPa, using the CHARMM36 and COMPASS force fields.

Multiple simulation cells are utilized to obtain partition coefficients in the DIPE + Ethanol + Water system. The cells differ in the number of water, DIPE, and ethanol molecules. This is necessary to obtain systems with varying ethanol concentrations in the phases.

For simulations with the CHARMM36 force field, cells are constructed using GROMACS utilities. The cell dimensions range from 6–9 nm along the x and y axes, and 11–17 nm along the z axis. Initially, a cell containing only DIPE molecules is created. Subsequently, it is symmetrically expanded three times in both directions along the z axis. During each expansion, new molecules are inserted into the cell: first water, then ethanol, and finally water again. After each expansion and molecule insertion, a 0.2 ns relaxation is performed in the NPT ensemble to allow the added layers to slightly compress. An example of a relaxed system for estimating solubility and the corresponding density distribution plot are presented in Fig. 5.

Upon completion of these procedures, a layered structure is formed within the cell: a central layer with a predominance of DIPE molecules (organic phase), flanked by two layers with a predominance of water molecules (aqueous phase), and ethanol molecules distributed among these two phases. Relaxation is carried out in the NPT ensemble for 1 ns, followed by the NVT ensemble for 0.5 ns. Subsequently, 30–50 ns NVT production calculations are performed. An example of a calculated density profile is presented in Fig. 5b.

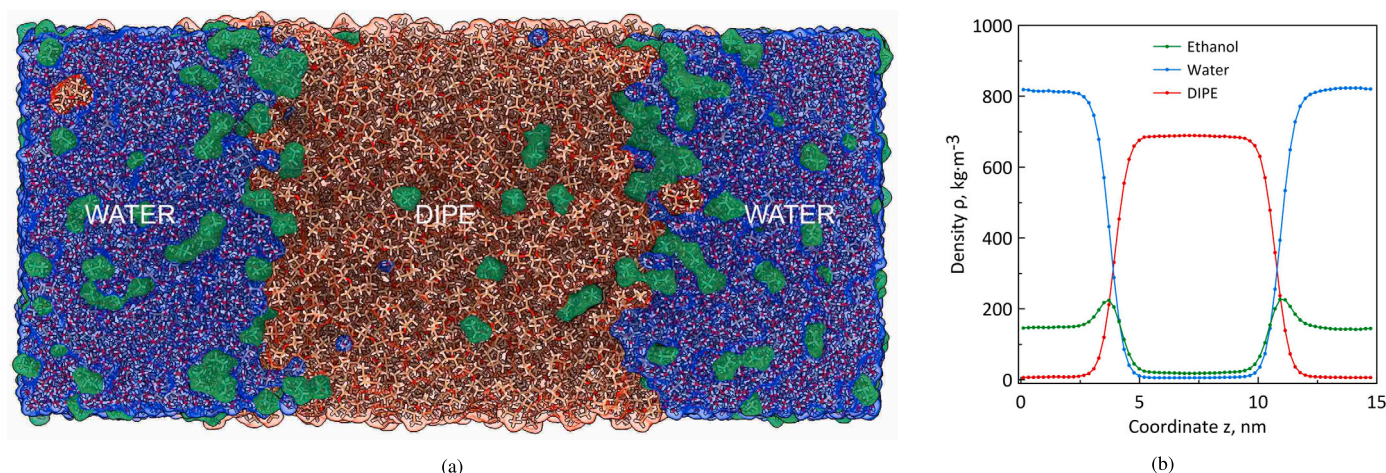


Fig. 5. (a) An example of a system for estimating a partition coefficient containing 1,248 DIPE (colored red), 949 ethanol (colored green), and 9,402 water (colored blue) molecules. The configuration is visualized in the UCSF ChimeraX [102]. (b) An example of an established density profile in ternary system for CHARMM36 at 298.15 K and 0.1 MPa.

For simulations with the COMPASS force field, the Moltemplate program is employed to generate the initial configuration of the molecules. The cell dimensions range from 6–9 nm along the x and y axes, and 12–20 nm along the z axis. The initial coordinates of the molecules are specified on a lattice. Analogous to the DIPE + Water system, a layer of DIPE molecules is positioned between two layers of water, and ethanol molecules are initially distributed uniformly throughout the cell. Cell relaxation is performed in the NPT ensemble for 2 ns, followed by a 4 ns NVT ensemble simulation for collecting statistical data on the density distribution along the z axis.

An interesting phenomenon observed during simulations with the CHARMM36 force field is the formation of stable water clusters within the organic phase for certain cells. The ethanol molecules also induce pronounced inhomogeneities in both the aqueous and organic phases. However, unlike water, ethanol does not form clusters, which can be attributed to the insufficient cell size for such an effect to manifest. The impact of inhomogeneities and clusters in liquid solutions is a topic of practical interest [110–113]. Such inhomogeneities can exert a noticeable influence on chemical processes [114].

Owing to these inhomogeneities, it is necessary to significantly extend the simulation time to ensure that all inhomogeneities are adequately averaged, and the density profile along the z axis attains a constant form in the regions corresponding to the aqueous and organic phases. However, in some cases, an increase of the simulation time fails to significantly reduce inhomogeneities influence. In such instances, the cell is discarded and a new simulation cell with modified dimensions is created.

For both force fields, the partition coefficients are calculated for several unit cells with varying ethanol concentrations. For COMPASS, the ethanol mole fractions in the organic phase c_1 range from 0.2 to 0.4. For CHARMM36, they range within 0.05–0.2. As a result of the calculations, two sets of partition coefficients are obtained. It is found that for COMPASS the results differ by no more than 10%. A similar observation holds for the values in the CHARMM36 results. Considering that the method can only provide estimations of concentrations, we present only an order-of-magnitude estimation for the obtained partition coefficients. As discussed in the previous section, such precision is sufficient for the intended comparison. The simulation results are presented in Table 1.

CHARMM36 yields partition coefficients of the same order of magnitude as the experimental values. COMPASS overestimates partition coefficients by an order of magnitude.

4. Discussion

In this study, using DIPE as a convenient model substance, we investigate the ability to simulate liquid ether-based membranes in MD. For this purpose, we evaluate the performance of the GAFF, OPLS-AA/CM1A, CHARMM36, and COMPASS force fields in reproducing the density and shear viscosity of DIPE, as well as the thermodynamic properties of the DIPE + Water and DIPE + Ethanol + Water solutions.

The GAFF and OPLS-AA/CM1A force fields yield similar results in predicting the density and shear viscosity of DIPE. Both force fields overestimate the density values by no more than 3–5% across the entire temperature range. These force fields also overestimate the shear viscosity by 50–70% at 293.15–333.15 K and by 70–130% at 243.15–283.15 K. The low accuracy in predicting density and especially viscosity suggests that GAFF and OPLS-AA/CM1A are not suitable for modeling ether-based liquid membranes.

The CHARMM36 force field describes the temperature dependency of DIPE density better than OPLS-AA/CM1A, but slightly worse than GAFF at higher temperatures. It yields an error of approximately 1% at 243.15–283.15 K and 1–4% at 293.15–333.15 K. Additionally, it provides a reasonably close agreement with experimental shear viscosity data. At 273.15–333.15 K, the error is about 10–20%, and at 283.15–333.15 K, it is 2–9%. Based on the results of estimating thermodynamic properties of solutions, CHARMM36 underestimates the solubility of DIPE in water by an order of magnitude and falls within the same order of magnitude for the solubility of water in DIPE and the partition coefficients of ethanol. CHARMM36 also yields close agreement with experimental data on interfacial tension between DIPE and water. The error is about 6%.

It can be concluded that CHARMM36 reproduces the DIPE density and shear viscosity at temperatures of approximately 293–333 K with reasonable accuracy. Furthermore, it yields satisfactory prediction quality for the thermodynamic properties of DIPE solution with water. This suggests that the CHARMM36 force field can be used to predict the properties of ether-based liquid membranes qualitatively.

The COMPASS force field yields the best accuracy in reproducing the density and shear viscosity of DIPE among all the considered force fields. Moreover, the agreement with experimental data improves with increasing temperature. For COMPASS, the prediction error for density decreases from 1% to 0.3%, and the prediction error for viscosity decreases from 6% to 1% as the temperature increases. However, when estimating thermodynamic properties of DIPE solution with water, COMPASS underestimates the solubility of DIPE in water by two orders of magnitude and the solubility of water in DIPE by one order of

magnitude. It also deviates by one order of magnitude when predicting partition coefficients. COMPASS reproduces a two times greater value of interfacial tension, than the experimental one.

Therefore, it can be stated that COMPASS yields excellent agreement with experimental values for the temperature dependencies of DIPE density and shear viscosity, surpassing all the other considered force fields in this regard. This allows us to conclude that COMPASS is the most suitable force field for modeling transport processes in pure ethers. However, COMPASS demonstrates poor prediction quality for the thermodynamic properties of DIPE solution with water. It yields a large error in reproducing the solubility and interfacial tension. That is why when using COMPASS for simulating the distribution of ions in a liquid membrane system, its good accuracy in reproducing transport properties will not play a significant role. Hence, its ability to accurately model transport processes in liquid membranes is questionable.

When comparing CHARMM36 and COMPASS, we can conclude that CHARMM36 reproduces the thermodynamic properties of the DIPE solution with water better than COMPASS. The slight advantage of COMPASS in the prediction accuracy of transport properties does not play a significant role in this case. Thus, CHARMM36 can be considered the best among the considered force fields for qualitative modeling of ion-selective barriers based on ethers.

Unlike COMPASS, the parameterization of CHARMM36 is more focused on describing organic substances in an aqueous environment. Therefore, the interaction of organic molecules with water is more accurately calibrated for CHARMM36. It allows CHARMM36 to better describe the thermodynamic properties of the DIPE + Water system.

5. Conclusions

In this work, we evaluate the applicability of force fields (GAFF, OPLS-AA/CM1A, CHARMM36 and COMPASS) for modeling properties of ether-based liquid membranes. The density and shear viscosity of DIPE are calculated over the temperature range of 243–333 K using these force fields. For CHARMM36 and COMPASS, the interfacial tension between DIPE and water is obtained, the mutual solubilities of DIPE and water, as well as the partition coefficients of ethanol in DIPE + Ethanol + Water systems, are estimated.

1. The GAFF and OPLS-AA/CM1A force fields do not provide the required modeling accuracy for both DIPE density and shear viscosity. Consequently, the force fields are not suitable for modeling ether-based selective barriers.
2. The COMPASS force field reproduces the density and shear viscosity of DIPE with excellent precision. However, it yields a substantial error when predicting interfacial tension and the mutual solubility of DIPE and water, as well as the partition coefficients of ethanol in DIPE + Ethanol + Water systems. In this regard, it can be expected that this force field will accurately predict the transport properties of ethers, but when modeling liquid membranes based on ethers, one can only anticipate a qualitative level of accuracy. Moreover, COMPASS is a proprietary force field, which further limits its use.
3. The CHARMM36 force field quite accurately reproduces DIPE density, DIPE shear viscosity, and interfacial tension between DIPE and water. Simultaneously, it qualitatively describes the thermodynamic properties of DIPE and its water solution. Therefore, CHARMM36 can be used to model ether-based selective barriers at a qualitative level.

Based on the comparison results, it can be concluded that CHARMM36 is the most suitable force field for qualitative modeling of liquid ether-based membranes. Having the parameters set for ions, it should be applied for the simulations of ion selectivity process in future research.

CRedit authorship contribution statement

Oleg V. Kashurin: Writing – review & editing, Writing – original draft, Visualization, Investigation, Formal analysis. **Nikolay D. Kondratyuk:** Software, Resources, Methodology, Funding acquisition. **Alexander V. Lankin:** Supervision, Investigation, Data curation, Conceptualization. **Genri E. Norman:** Project administration, Conceptualization.

Supplementary material

The files for carrying out the simulations in all the force fields are available on [GitHub](#).

Declaration of competing interest

The authors declare that they have no known competing financial interests or personal relationships that could have appeared to influence the work reported in this paper.

Acknowledgements

This work is supported by the strategic academic leadership program “Priority-2030” (Agreement 075-15-2024-200 06.02.2024) – O.V. Kashurin (calculations, analysis of results, writing the text of the paper), N.D. Kondratyuk (calculation methods, analysis of results, resources) and A.V. Lankin (problem statement, analysis of results, literature review), and with financial support from the Ministry of Science and Higher Education of the Russian Federation (Agreement No. 075-01129-23-00) – G. E. Norman (structure of the paper). N.D.K. and G.E.N. gratefully acknowledge support from the framework of the HSE University Basic Research Program.

The calculations are performed on the *Soft Cluster* of the Laboratory of Multiscale Modeling in Soft Matter Physics, on the MIPT cluster, and on the *Fisher* and *Desmos* supercomputers [85,86] of the Joint Institute for High Temperatures of RAS.

Data availability

Data will be made available on request.

References

- [1] H. Bukowsky, E. Uhlemann, Selective extraction of lithium chloride from brines, Sep. Sci. Technol. 28 (6) (1993) 1357–1360, <https://doi.org/10.1080/01496399308018042>.
- [2] J. Xiao, Y. Jia, C. Shi, X. Wang, S. Wang, Y. Yao, Y. Jing, Lithium isotopes separation by using benzo-15-crown-5 in eco-friendly extraction system, J. Mol. Liq. 241 (Sep. 2017), <https://doi.org/10.1016/j.molliq.2017.06.119>.
- [3] G. Liu, Z. Zhao, A. Ghahreman, Novel approaches for lithium extraction from salt-lake brines: a review, Hydrometallurgy 187 (2019) 81–100, <https://doi.org/10.1016/j.hydromet.2019.05.005>.
- [4] W. Chen, C. Zhao, B. Li, Q. Jin, X. Zhang, T. Yuan, X. Zhang, Z. Jin, S. Kaskel, Q. Zhang, A mixed ether electrolyte for lithium metal anode protection in working lithium–sulfur batteries, Energy Environ. Mater. 3 (2) (2020) 160–165, <https://doi.org/10.1002/eeem.2.12073>.
- [5] X. Zhang, Q. Jin, Y. Nan, L. Hou, B. Li, X. Chen, Z. Jin, X. Zhang, J. Huang, Q. Zhang, Electrolyte structure of lithium polysulfides with anti-reductive solvent shells for practical lithium–sulfur batteries, Angew. Chem., Int. Ed. Engl. 60 (28) (2021) 15503–15509, <https://doi.org/10.1002/anie.202103470>.
- [6] Y. Sun, Q. Wang, Y. Wang, R. Yun, X. Xiang, Recent advances in magnesium/lithium separation and lithium extraction technologies from salt lake brine, Sep. Purif. Technol. 256 (2021) 117807, <https://doi.org/10.1016/j.seppur.2020.117807>.
- [7] C. Zhang, L. Zhang, Y. Ding, S. Peng, X. Guo, Y. Zhao, G. He, G. Yu, Progress and prospects of next-generation redox flow batteries, Energy Stor. Mater. 15 (2018) 324–350, <https://doi.org/10.1016/j.ensm.2018.06.008>.
- [8] E. Hendriks, G.M. Kontogeorgis, R. Dohn, J.-C. de Hemptinne, I.G. Economou, L.F. Zilnik, V. Vesovic, Industrial requirements for thermodynamics and transport properties, Industrial & engineering chemistry research 49 (22) (2010) 11131–11141.

- [9] G.M. Kontogeorgis, R. Dohrn, I.G. Economou, J.-C. de Hemptinne, A. Ten Kate, S. Kuitunen, M. Mooijer, L.F. Žilnik, V. Vesovic, Industrial requirements for thermodynamic and transport properties: 2020, *Industrial & engineering chemistry research* 60 (13) (2021) 4987–5013.
- [10] M. Tillotson, N. Diamantonis, C. Buda, L. Bolton, E. Müller, Molecular modelling of the thermophysical properties of fluids: expectations, limitations, gaps and opportunities, *physical chemistry chemical physics*, PCCP 25 (Apr. 2023), <https://doi.org/10.1039/d2cp05423j>.
- [11] I.K. Bakulin, I.V. Kopanichuk, N.D. Kondratyuk, Molecular-level insights to structure and hydrogen bonds network of 1, 4-dioxane aqueous solution, *Journal of Molecular Liquids* 393 (2024) 123523, <https://doi.org/10.1016/j.molliq.2023.123523>.
- [12] B. Zêzere, I. Portugal, C. Silva, J. Gomes, Diffusivities of ketones and aldehydes in liquid ethanol by molecular dynamics simulations, *J. Mol. Liq.* 371 (2023) 121068, <https://doi.org/10.1016/j.molliq.2022.121068>.
- [13] X. Dingcheng, D. Yipan, W. Zhenyao, L. Tianhao, L. Yinshui, Viscosity evolution of water glycol in deep-sea environment at high pressure and low temperature, *J. Mol. Liq.* 387 (2023) 122387, <https://doi.org/10.1016/j.molliq.2023.122387>.
- [14] N. Orekhov, N. Kondratyuk, M. Logunov, A. Timralieva, V. Shilovskikh, E. Skorb, Insights into the early stages of melamine cyanurate nucleation from aqueous solution, *Cryst. Growth Des.* 21 (4) (2021) 1984–1992, <https://doi.org/10.1021/acs.cgd.0c01285>.
- [15] O.V. Grineva, E.V. Belyaeva, Structure of water-glycine solutions in saturated and near-saturated regions according to compressibility data, *J. Struct. Chem.* 52 (6) (2011) 1139–1143, <https://doi.org/10.1134/S0022476611060199>.
- [16] X. Chen, H. Zhang, H. Yokoyama, W. Woei, Fong Chong, K. Fukuzawa, S. Itoh, Molecular dynamics study of confined liquid film viscosity in constant-pressure and constant-distance systems, *Journal of Molecular Liquids* 404 (2024) 124955, <https://doi.org/10.1016/j.molliq.2024.124955>.
- [17] Z. Zhang, M. Joy, S. Vanapalli, Experimental and theoretical analysis of solute redistribution during a progressive freeze concentration process, *Int. Commun. Heat Mass* 152 (2024) 107288, <https://doi.org/10.1016/j.icheatmasstransfer.2024.107288>.
- [18] A. Gupta, S. Gohil, Insights into structural difference between sodium polyacrylate PAA and sodium polymethacrylate PMA in salt solutions investigated by molecular simulations, *J. Mater. Sci.* 57 (23) (2022) 10569–10584, <https://doi.org/10.1007/s10853-021-06836-8>.
- [19] M. Zhou, K. Cheng, G. Jia, Molecular dynamics simulation studies of dopamine aqueous solution, *J. Mol. Liq.* 230 (2017) 137–142, <https://doi.org/10.1016/j.molliq.2016.11.079>.
- [20] H.C. Visser, D.N. Reinhoudt, F. Jong, Carrier-mediated transport through liquid membranes, *Chem. Soc. Rev.* 23 (2) (1994) 75–81, <https://doi.org/10.1039/CS9942300075>.
- [21] M. Blahůš, F. Marták, F. Miranda, S. Schlosser, J. Teixeira, Effect of viscosity of a liquid membrane containing oleyl alcohol on the pertraction of butyric acid, *Chemical Papers* 67 (12) (2013) 1560–1568, <https://doi.org/10.2478/s11696-013-0370-4>.
- [22] R. Fortunato, C.A.M. Afonso, M.A.M. Reis, J.G. Crespo, Supported liquid membranes using ionic liquids: study of stability and transport mechanisms, *Journal of Membrane Science* 242 (1) (2004) 197–209, <https://doi.org/10.1016/j.memsci.2003.07.028>.
- [23] S. Pavón, A. Fortuny, M.T. Coll, M. Bertau, A.M. Sastre, Permeability dependencies on the carrier concentration and membrane viscosity for Y(III) and Eu(III) transport by using liquid membranes, *Separation and Purification Technology* 239 (2020) 116573, <https://doi.org/10.1016/j.seppur.2020.116573>.
- [24] H. Takeuchi, K. Takahashi, W. Goto, Some observations on the stability of supported liquid membranes, *Journal of Membrane Science* 34 (1) (1987) 19–31, [https://doi.org/10.1016/S0376-7388\(00\)80018-6](https://doi.org/10.1016/S0376-7388(00)80018-6).
- [25] X. Meng, J. Wu, Z. Liu, Viscosity and density measurements of diisopropyl ether and dibutyl ether at different temperatures and pressures, *J. Chem. Eng. Data* 54 (9) (2009) 2353–2358, <https://doi.org/10.1021/jc8005369>.
- [26] D. Montañó, H. Guerrero, I. Bandrés, M. López, C. Lafuente, Viscosities of binary mixtures containing isomeric chlorobutanes and diisopropylether: experimental and predicted values, *Int. J. Thermophys.* 31 (3) (2010) 488–501, <https://doi.org/10.1007/s10765-010-0737-5>.
- [27] S. Ahmadi, M. Almasi, Experimental and modeling study of diisopropyl ether and 2-alkanol/PC-SAFT model and free volume theory, *J. Chem. Thermodyn.* 142 (2020) 106025, <https://doi.org/10.1016/j.jct.2019.106025>.
- [28] F. Frere, Ternary system diisopropyl ether–isopropyl alcohol–water at 25 °C, *Ind. Eng. Chem.* 41 (10) (1949) 2365–2367, <https://doi.org/10.1021/ie50478a065>.
- [29] K. Ye, J. Wu, G. Deng, Liquid–liquid equilibria of ternary mixture (propargyl alcohol+diisopropyl ether+water), *Fluid Phase Equilib.* 260 (2) (2007) 262–265, <https://doi.org/10.1016/j.fluid.2007.07.015>.
- [30] A. Arce, A. Marchiaro, O. Rodríguez, A. Soto, Liquid-liquid equilibrium of diisopropyl ether + ethanol + water system at different temperatures, *J. Chem. Eng. Data* 47 (3) (2002) 529–532, <https://doi.org/10.1021/jc010297w>.
- [31] I. Hwang, S. Park, J. Choi, Liquid-liquid equilibria for the binary system of diisopropyl ether (DIPE)+water in between 288.15 and 323.15 K and the ternary systems of DIPE+water+C1–C4 alcohols at 298.15 K, *Fluid Phase Equilib.* 269 (1–2) (2008) 1–5, <https://doi.org/10.1016/j.fluid.2008.04.010>.
- [32] H. Cárdenas, M. Cartes, A. Mejía, Atmospheric densities and interfacial tensions for 1-alkanol (1-butanol to 1-octanol)+water and ether (MTBE, ETBE, DIPE, TAME and THP)+water demixed mixtures, *Fluid Phase Equilibria* 396 (2015) 88–97, <https://doi.org/10.1016/j.fluid.2015.03.040>.
- [33] S. Schmitt, F. Fleckenstein, H. Hasse, S. Stephan, Comparison of force fields for the prediction of thermophysical properties of long linear and branched alkanes, *J. Phys. Chem. B* 127 (8) (2023) 1789–1802, <https://doi.org/10.1021/acs.jpcc.2c07997>.
- [34] J. Ewen, C. Gattinoni, F. Thakkar, N. Morgan, H. Spikes, D. Dini, A comparison of classical force-fields for molecular dynamics simulations of lubricants, *Materials* 9 (8) (2016) 651, <https://doi.org/10.3390/ma9080651>.
- [35] A. Glova, I. Volgin, V. Nazarychev, S. Larin, S. Lyulin, A. Gurtovenko, Toward realistic computer modeling of paraffin-based composite materials: critical assessment of atomic-scale models of paraffins, *RSC Adv.* 9 (66) (2019) 38834–38847, <https://doi.org/10.1039/C9RA07325F>.
- [36] N. Orekhov, G. Ostroumova, V. Stegailov, High temperature pure carbon nanoparticle formation: validation of AIREBO and ReaxFF reactive molecular dynamics, *Carbon* 170 (2020) 606–620, <https://doi.org/10.1016/j.carbon.2020.08.009>.
- [37] V. Nazarychev, A. Glova, I. Volgin, S. Larin, A. Lyulin, S. Lyulin, A. Gurtovenko, Evaluation of thermal conductivity of organic phase-change materials from equilibrium and non-equilibrium computer simulations: paraffin as a test case, *Int. J. Heat Mass Transfer* 165 (Feb. 2021), <https://doi.org/10.1016/j.ijheatmasstransfer.2020.120639>.
- [38] V. Deschenya, N. Kondratyuk, A. Lankin, G. Norman, Molecular dynamics study of sucrose aqueous solutions: from solution structure to transport coefficients, *J. Mol. Liq.* 367 (2022) 120456, <https://doi.org/10.1016/j.molliq.2022.120456>.
- [39] R. Atwi, N.N. Rajput, Guiding maps of solvents for lithium-sulfur batteries via a computational data-driven approach, *Patterns* 4 (9) (2023) 100799, <https://doi.org/10.1016/j.patter.2023.100799>.
- [40] S.E. Brandolin, J.A. Scilipoti, I. Magario, Elucidating solvent effects on lipase-catalyzed peroxyacid synthesis through activity-based kinetics and molecular dynamics, *Biotechnology and Bioengineering* 121 (9) (2024) 2728–2741, <https://doi.org/10.1002/bit.28762>.
- [41] W. Jorgensen, D. Maxwell, J. Tirado-Rives, Development and testing of the OPLS all-atom force field on conformational energetics and properties of organic liquids, *J. Am. Chem. Soc.* 118 (45) (1996) 11225–11236, <https://doi.org/10.1021/ja9621760>.
- [42] W. Jorgensen, J. Tirado-Rives, Potential energy functions for atomic-level simulations of water and organic and biomolecular systems, *Proc. Natl. Acad. Sci. U. S. A.* 102 (19) (2005) 6665–6670, <https://doi.org/10.1073/pnas.0408037102>.
- [43] J. Wang, R. Wolf, J. Caldwell, P. Kollman, D. Case, Development and testing of a general amber force field, *J. Comput. Chem.* 25 (9) (2004) 1157–1174, <https://doi.org/10.1002/jcc.20035>.
- [44] L. Dodda, J. Vilseck, J. Tirado-Rives, W. Jorgensen, 1.14*CM1A-LBCC: localized bond-charge corrected CM1A charges for condensed-phase simulations, *J. Phys. Chem. B* 121 (15) (2017) 3864–3870, <https://doi.org/10.1021/acs.jpcc.7b00272>.
- [45] J.B. Klauda, V.M. Richard, J.A. Freites, J.W. O'Connor, T.J. Douglas, C. Mondragon-Ramirez, I. Vorobyov, A.D.J. MacKerell, R.W. Pastor, Update of the CHARMM all-atom additive force field for lipids: validation on six lipid types, *J. Phys. Chem. B* 114 (23) (2010) 7830–7843, <https://doi.org/10.1021/jp101759q>.
- [46] A.D.J. MacKerell, D. Bashford, M. Bellott, R.L.J. Dunbrack, J.D. Evanseck, M.J. Field, S. Fischer, J. Gao, H. Guo, S. Ha, D. Joseph-McCarthy, L. Kuchner, K. Kuczyra, F.T.K. Lau, C. Mattos, S. Michnick, T. Ngo, D.T. Nguyen, B. Prodhom, W.E. Reiher, B. Roux, M. Schlenkerich, J.C. Smith, R. Stote, J. Straub, M. Watanabe, J. Wiórkiewicz-Kuczera, D. Yin, M. Karplus, All-atom empirical potential for molecular modeling and dynamics studies of proteins, *J. Phys. Chem. B* 102 (18) (Apr. 1998), <https://doi.org/10.1021/jp973084f>.
- [47] H. Sun, COMPASS: an ab initio force-field optimized for condensed-phase Applications Overview with details on alkane and benzene compounds, *J. Phys. Chem. B* 102 (38) (1998) 7338–7364, <https://doi.org/10.1021/jp980939v>.
- [48] J.R. Maple, M.-J. Hwang, T.P. Stockfisch, U. Dinur, M. Waldman, C.S. Ewig, A.T. Hagler, Derivation of class ii force fields. I. Methodology and quantum force field for the alkyl functional group and alkane molecules, *Journal of Computational Chemistry* 15 (2) (1994) 162–182.
- [49] R. David, Fluid density predictions using the COMPASS force field, *Fluid Ph. Equilibria* 217 (1) (2004) 77–87, <https://doi.org/10.1016/j.fluid.2003.08.019>.
- [50] N.D. Kondratyuk, V.V. Pisarev, Calculation of viscosities of branched alkanes from 0.1 to 1000 MPa by molecular dynamics methods using COMPASS force field, *Fluid Ph. Equilibria* 498 (2019) 151–159, <https://doi.org/10.1016/j.fluid.2019.06.023>.
- [51] Y. Yu, A. Krämer, R.M. Venable, A.C. Simmonett, A.D.J. MacKerell, J.B. Klauda, R.W. Pastor, B.R. Brooks, Semi-automated optimization of the CHARMM36 lipid force field to include explicit treatment of long-range dispersion, *J. Chem. Theory Comput.* 17 (3) (2021) 1562–1580, <https://doi.org/10.1021/acs.jctc.0c01326>.
- [52] A.N. Leonard, R.W. Pastor, J.B. Klauda, Parameterization of the CHARMM all-atom force field for ether lipids and model linear ethers, *J. Phys. Chem. B* 122 (26) (2018) 6744–6754, <https://doi.org/10.1021/acs.jpcc.8b02743>.
- [53] Y. Yu, R.M. Venable, J. Thirman, P. Chatterjee, A. Kumar, R.W. Pastor, B. Roux, A.D.J. MacKerell, J.B. Klauda, Drude polarizable lipid force field with explicit treatment of long-range dispersion: parametrization and validation for saturated and monounsaturated zwitterionic lipids, *J. Chem. Theory Comput.* 19 (9) (2023) 2590–2605, <https://doi.org/10.1021/acs.jctc.3c00203>.

- [54] K. Vanommeslaeghe, E. Hatcher, C. Acharya, S. Kundu, S. Zhong, J. Shim, E. Darian, O. Guvench, P. Lopes, I. Vorobyov, A.D. Mackerell Jr., CHARMM general force field: a force field for drug-like molecules compatible with the CHARMM all-atom additive biological force fields, *Journal of Computational Chemistry* 31 (4) (2010) 671–690, <https://doi.org/10.1002/jcc.21367>.
- [55] M. Waldman, A. Hagler, New combining rules for rare gas van der Waals parameters, *J. Comput. Chem.* 14 (9) (1993) 1077–1084, <https://doi.org/10.1002/jcc.540140909>.
- [56] J. Wang, W. Wang, P. Kollman, D. Case, Automatic atom type and bond type perception in molecular mechanical calculations, *J. Mol. Graphics Modell.* 25 (2) (2006) 247–260, <https://doi.org/10.1016/j.jmngm.2005.12.005>.
- [57] R. Walker, M. Crowley, D. Case, The implementation of a fast and accurate QM/MM potential method in Amber, *J. Comput. Chem.* 29 (7) (2008) 1019–1031, <https://doi.org/10.1002/jcc.20857>.
- [58] L. Dodda, I. Cabeza de Vaca, J. Tirado-Rives, W. Jorgensen, LigParGen web server: an automatic OPLS-AA parameter generator for organic ligands, *Nucleic Acids Res.* 45 (W1) (2017) W331–W336, <https://doi.org/10.1093/nar/gkx312>.
- [59] S. Jo, T. Kim, V. Iyer, W. Im, CHARMM-GUI: a web-based graphical user interface for CHARMM, *J. Comput. Chem.* 29 (11) (2008) 1859–1865, <https://doi.org/10.1002/jcc.20945>.
- [60] B. Brooks, C. Brooks, A. MacKerell, L. Nilsson, R. Petrella, B. Roux, Y. Won, G. Archontis, C. Bartels, S. Boresch, A. Caflisch, L. Caves, Q. Cui, A. Dinner, M. Feig, S. Fischer, J. Gao, M. Hodoseck, W. Im, K. Kuczera, T. Lazaridis, J. Ma, V. Ovchinnikov, E. Paci, R. Pastor, C. Post, J. Pu, M. Schaefer, B. Tidor, R.M. Venable, H.L. Woodcock, X. Wu, W. Yang, D. York, M. Karplus, CHARMM: the biomolecular simulation program, *J. Comput. Chem.* 30 (10) (2009) 1545–1614, <https://doi.org/10.1002/jcc.21287>.
- [61] J. Lee, X. Cheng, J.M. Swails, M.S. Yeom, P.K. Eastman, J.A. Lemkul, S. Wei, J. Buckner, J.C. Jeong, Y. Qi, S. Jo, V.S. Pande, D.A. Case, C.L.I. Brooks, A.D.J. MacKerell, J.B. Klauda, W. Im, CHARMM-GUI input generator for NAMD, GROMACS, AMBER, OpenMM, and CHARMM/OpenMM simulations using the CHARMM36 additive force field, *J. Chem. Theory Comput.* 12 (1) (2016) 405–413, <https://doi.org/10.1021/acs.jctc.5b00935>.
- [62] COMPASS parameters at the LAMMPS github, https://github.com/lammps/lammps/blob/develop/tools/msi2lmp/frc_files/compass_published.frc (Accessed 18 October 2023).
- [63] S. Boonstra, P. Onck, E. van der Giessen, CHARMM TIP3P water model suppresses peptide folding by solvating the unfolded state, *J. Phys. Chem. B* 120 (15) (2016) 3692–3698, <https://doi.org/10.1021/acs.jpcc.6b01316>.
- [64] E. Ong, J. Liow, The temperature-dependent structure, hydrogen bonding and other related dynamic properties of the standard TIP3P and CHARMM-modified TIP3P water models, *Fluid Phase Equilib.* 481 (2019) 55–65, <https://doi.org/10.1016/j.fluid.2018.10.016>.
- [65] H. Heinz, T. Lin, R. Kishore Mishra, F.S. Emami, Thermodynamically consistent force fields for the assembly of inorganic, organic, and biological nanostructures: the INTERFACE force field, *Langmuir* 29 (6) (2013) 1754–1765, <https://doi.org/10.1021/la3038846>.
- [66] S.P. Kadaoluwa Pathirannahalag, N. Meftahi, A. Elbourne, A.C.G. Weiss, C.F. McConville, A. Padua, D.A. Winkler, M. Costa Gomes, T.L. Greaves, Q.A. Besford, T.C. Le, A.J. Christofferson, A systematic comparison of the structural and dynamic properties of commonly used water models for molecular dynamics simulations, preprint Chemistry, Jul. 2021, <https://doi.org/10.26434/chemrxiv-2021-0dt3n>.
- [67] M. Abraham, T. Murtola, R. Schulz, S. Páll, J. Smith, B. Hess, E. Lindahl, GROMACS: high performance molecular simulations through multi-level parallelism from laptops to supercomputers, *SoftwareX* 1–2 (2015) 19–25, <https://doi.org/10.1016/j.softx.2015.06.001>.
- [68] S. Páll, M.J. Abraham, C. Kutzner, B. Hess, E. Lindahl, Tackling exascale software challenges in molecular dynamics simulations with GROMACS, in: S. Markidis, E. Laure (Eds.), *Solving Software Challenges for Exascale*, Springer International Publishing, Cham, 2015, pp. 3–27.
- [69] S. Pronk, S. Páll, R. Schulz, P. Larsson, P. Bjelkmar, R. Apostolov, M. Shirts, J. Smith, P. Kasson, D. van der Spoel, B. Hess, E. Lindahl, GROMACS 4.5: a high-throughput and highly parallel open source molecular simulation toolkit, *Bioinformatics* 29 (7) (Apr. 2013), <https://doi.org/10.1093/bioinformatics/btt055>.
- [70] A.P. Thompson, H.M. Aktulga, R. Berger, D.S. Bolintineanu, W.M. Brown, P.S. Crozier, P.J. in 't Veld, A. Kohlmeyer, S.G. Moore, T.D. Nguyen, R. Shan, M.J. Stevens, J. Tranchida, C. Trott, S.J. Plimpton, LAMMPS - a flexible simulation tool for particle-based materials modeling at the atomic, meso, and continuum scales, *Comput. Phys. Commun.* 271 (2022) 108171, <https://doi.org/10.1016/j.cpc.2021.108171>.
- [71] W. Brown, P. Wang, S. Plimpton, A. Tharrington, Implementing molecular dynamics on hybrid high performance computers - short range forces, *Comput. Phys. Commun.* 182 (2011) 898–911, <https://doi.org/10.1016/j.cpc.2010.12.021>.
- [72] W. Brown, A. Kohlmeyer, S. Plimpton, A. Tharrington, Implementing molecular dynamics on hybrid high performance computers - particle-particle particle-mesh, *Comput. Phys. Commun.* 183 (2012) 449–459, <https://doi.org/10.1016/j.cpc.2011.10.012>.
- [73] S.A. Burrows, I. Korotkin, S.K. Smoukov, E. Boek, S. Karabasov, Benchmarking of molecular dynamics force fields for solid–liquid and solid–solid phase transitions in alkanes, *J. Phys. Chem. B* 125 (19) (2021) 5145–5159.
- [74] D. Frenkel, B. Smit, *Understanding Molecular Simulations*, 2nd edition, Academic Press, San Diego, 2001.
- [75] S. Werth, G. Rutkai, J. Vrabec, M. Horsch, H. Hasse, Long-range correction for multi-site Lennard-Jones models and planar interfaces, *Mol. Phys.* 112 (17) (2014) 2227–2234.
- [76] S. Stephan, H. Hasse, Influence of dispersive long-range interactions on properties of vapour–liquid equilibria and interfaces of binary Lennard-Jones mixtures, *Mol. Phys.* 118 (9–10) (2020) e1699185.
- [77] R.W. Hockney, J.W. Eastwood, *Computer Simulation Using Particles*, A. Hilger, Bristol [England], Philadelphia, 1988.
- [78] E. Pollock, J. Glosli, Comments on P3M, FMM, and the Ewald method for large periodic coulombic systems, *Comput. Phys. Commun.* 95 (2) (1996) 93–110, [https://doi.org/10.1016/0010-4655\(96\)00043-4](https://doi.org/10.1016/0010-4655(96)00043-4).
- [79] U. Essmann, L. Perera, M. Berkowitz, T. Darden, H. Lee, L. Pedersen, A smooth particle mesh Ewald method, *J. Chem. Phys.* 103 (19) (1995) 8577–8593, <https://doi.org/10.1063/1.470117>.
- [80] S. Nosé, A molecular dynamics method for simulations in the canonical ensemble, *Mol. Phys.* 52 (2) (1984) 255–268, <https://doi.org/10.1080/00268978400101201>.
- [81] W. Hoover, Canonical dynamics: equilibrium phase-space distributions, *Phys. Rev. A* 31 (3) (1985) 1695–1697, <https://doi.org/10.1103/PhysRevA.31.1695>.
- [82] W. Shinoda, M. Shiga, M. Mikami, Rapid estimation of elastic constants by molecular dynamics simulation under constant stress, *Phys. Rev. B* 69 (13) (2004) 134103, <https://doi.org/10.1103/PhysRevB.69.134103>.
- [83] M. Bernetti, G. Bussi, Pressure control using stochastic cell rescaling, *J. Chem. Phys.* 153 (2020) 114107, <https://doi.org/10.1063/5.0020514>.
- [84] G. Bussi, D. Donadio, M. Parrinello, Canonical sampling through velocity rescaling, *J. Chem. Phys.* 126 (1) (2007) 014101, <https://doi.org/10.1063/1.2408420>.
- [85] N. Kondratyuk, V. Nikolskiy, D. Pavlov, V. Stegailov, GPU-accelerated molecular dynamics: state-of-art software performance and porting from Nvidia CUDA to AMD HIP, *Int. J. High Perform. Comput. Appl.* 35 (4) (2021) 312–324, <https://doi.org/10.1177/10943420211008288>.
- [86] V. Stegailov, E. Dlinnova, T. Ismagilov, M. Khalilov, N. Kondratyuk, D. Makagon, A. Semenov, A. Simonov, G. Smirnov, A. Timofeev, Angara interconnect makes GPU-based Desmos supercomputer an efficient tool for molecular dynamics calculations, *Int. J. High Perform. Comput. Appl.* 33 (3) (2019) 507–521, <https://doi.org/10.1177/1094342019826667>.
- [87] M. Jonsson, Standard error estimation by an automated blocking method, *Phys. Rev. E* 98 (4) (2018) 043304, <https://doi.org/10.1103/PhysRevE.98.043304>, publisher: American Physical Society.
- [88] M. Schappals, A. Mecklenfeld, L. Kröger, V. Botan, A. Köster, S. Stephan, E.J. García, G. Rutkai, G. Raabe, P. Klein, K. Leonhard, C.W. Glass, J. Lenhard, J. Vrabec, H. Hasse, Round Robin study: molecular simulation of thermodynamic properties from models with internal degrees of freedom, *J. Chem. Theory Comput.* 13 (9) (2017) 4270–4280, <https://doi.org/10.1021/acs.jctc.7b00489>.
- [89] N.M. Evstigneev, O.I. Ryabkov, K.M. Gerke, Stationary Stokes solver for single-phase flow in porous media: a blazingly fast solution based on algebraic multigrid method using gpu, *Adv. Water Resour.* 171 (2023) 104340.
- [90] S. Bair, T. Harris, A universal mixing rule for the high-pressure viscosity of oil/refrigerant mixtures, *J. Tribol.* (2023) 1–7.
- [91] D.A. Kulygin, A. Khlyupin, A. Cherkasov, R.A. Sirazov, D. Gafurova, Y.I. Gilmanov, K.V. Toropov, D.V. Korost, K.M. Gerke, Pore-scale simulations help in overcoming laboratory limitations with unconsolidated rock material: a multi-step reconstruction based on scanning electron and optical microscopy data, *Adv. Water Resour.* 190 (2024) 104754, <https://doi.org/10.1016/j.advwatres.2024.104754>.
- [92] G. Khnkoian, V. Nikolaev, V. Stegailov, Towards atomistic modelling of solid Pb-O formation and dissolution in liquid lead coolant: interatomic potential development, *J. Nucl. Mater.* 594 (2024) 155016.
- [93] M. Green, Markoff random processes and the statistical mechanics of time-dependent phenomena. II. Irreversible processes in fluids, *J. Chem. Phys.* 22 (3) (2004) 398–413, <https://doi.org/10.1063/1.1740082>.
- [94] R. Kubo, Statistical-mechanical theory of irreversible processes. I. General theory and simple applications to magnetic and conduction problems, *J. Phys. Soc. Jpn.* 12 (6) (1957) 570–586, <https://doi.org/10.1143/JPSJ.12.570>.
- [95] I.-C. Yeh, G. Hummer, System-size dependence of diffusion coefficients and viscosities from molecular dynamics simulations with periodic boundary conditions, *J. Phys. Chem. B* 108 (40) (2004) 15873–15879, <https://doi.org/10.1021/jp0477147>.
- [96] K.-S. Kim, M. Han, C. Kim, Z. Li, G. Karniadakis, E. Lee, Nature of intrinsic uncertainties in equilibrium molecular dynamics estimation of shear viscosity for simple and complex fluids, *J. Chem. Phys.* 149 (4) (2018) 044510, <https://doi.org/10.1063/1.5035119>.
- [97] Y. Zhang, A. Otani, E. Maginn, Reliable viscosity calculation from equilibrium molecular dynamics simulations: a time decomposition method, *J. Chem. Theory Comput.* 11 (8) (2015) 3537–3546, <https://doi.org/10.1021/acs.jctc.5b00351>.
- [98] E.J. Maginn, R.A. Messerly, D.J. Carlson, D.R. Roe, J.R. Elliot, Best practices for computing transport properties 1. self-diffusivity and viscosity from equilibrium molecular dynamics [article v1. 0], *Living J. Comput. Mol. Sci.* 1 (1) (2019) 6324–6343.
- [99] G. Toraman, T. Verstraeten, D. Fauconnier, Impact of ad hoc post-processing parameters on the lubricant viscosity calculated with equilibrium molecular dy-

- namics simulations, *Lubricants* 11 (4) (2023) 183–202, <https://doi.org/10.3390/lubricants11040183>.
- [100] E. Gine, J. Zinn, Bootstrapping general empirical measures, *Ann. Probab.* 18 (2) (1990) 851–869.
- [101] J. De Guzman, Relation between fluidity and heat of fusion, *An. Soc. Esp. Fis. Quim.* 11 (1913) 353–362.
- [102] E.F. Pettersen, T.D. Goddard, C.C. Huang, E.C. Meng, G.S. Couch, T.I. Croll, J.H. Morris, T.E. Ferrin, Ucsf chimeraX: structure visualization for researchers, educators, and developers, *Protein Sci.* 30 (1) (2021) 70–82.
- [103] A.I. Jewett, D. Stelter, J. Lambert, S.M. Saladi, O.M. Roscioni, M. Ricci, L. Autin, M. Maritan, S.M. Bashusqeh, T. Keyes, R.T. Dame, J.E. Shea, G.J. Jensen, D.S. Goodsell, Moltemplate: a tool for coarse-grained modeling of complex biological matter and soft condensed matter physics, *J. Mol. Biol.* 433 (11) (2021) 166841, <https://doi.org/10.1016/j.jmb.2021.166841>.
- [104] Y. Zhang, S.E. Feller, B.R. Brooks, R.W. Pastor, Computer simulation of liquid/liquid interfaces. I. Theory and application to octane/water, *J. Chem. Phys.* 103 (23) (1995) 10252–10266, <https://doi.org/10.1063/1.469927>.
- [105] S.E. Feller, Y. Zhang, R.W. Pastor, B.R. Brooks, Constant pressure molecular dynamics simulation: the Langevin piston method, *J. Chem. Phys.* 103 (11) (1995) 4613–4621, <https://doi.org/10.1063/1.470648>.
- [106] E.A. Müller, A. Mejía, Resolving discrepancies in the measurements of the interfacial tension for the CO₂ + H₂O mixture by computer simulation, *J. Phys. Chem. Lett.* 5 (7) (2014) 1267–1271, <https://doi.org/10.1021/jz500417w>.
- [107] C. Herdes, A. Ervik, A. Mejía, E.A. Müller, Prediction of the water/oil interfacial tension from molecular simulations using the coarse-grained SAFT- γ Mie force field, *Fluid Phase Equilib.* 476 (2018) 9–15, <https://doi.org/10.1016/j.fluid.2017.06.016>.
- [108] K.D. Papavasileiou, O.A. Moulton, I.G. Economou, Predictions of water/oil interfacial tension at elevated temperatures and pressures: a molecular dynamics simulation study with biomolecular force fields, *Fluid Phase Equilib.* 476 (2018) 30–38, <https://doi.org/10.1016/j.fluid.2017.05.004>.
- [109] E.A. Müller, A. Ervik, A. Mejía, A guide to computing interfacial properties of fluids from molecular simulations [article v1.0], *Living J. Comput Mol. Sci.* 2 (1) (2020), <https://doi.org/10.33011/livecoms.2.1.21385>.
- [110] S. Stephan, H. Cárdenas, A. Mejía, E.A. Müller, The monotonicity behavior of density profiles at vapor-liquid interfaces of mixtures, *Fluid Phase Equilib.* 564 (2023) 113596, <https://doi.org/10.1016/j.fluid.2022.113596>.
- [111] J.M. Garrido, M.M. Piñeiro, A. Mejía, F.J. Blas, Understanding the interfacial behavior in isopycnic Lennard-Jones mixtures by computer simulations, *Phys. Chem. Chem. Phys.* 18 (2) (2015) 1114–1124, <https://doi.org/10.1039/C5CP06562C>, publisher: The Royal Society of Chemistry.
- [112] S. Stephan, H. Hasse, Enrichment at vapour–liquid interfaces of mixtures: establishing a link between nanoscopic and macroscopic properties, *Int. Rev. Phys. Chem.* 39 (3) (2020) 319–349, <https://doi.org/10.1080/0144235X.2020.1777705>.
- [113] D. Rak, M. Sedláč, Solvophobicity-driven mesoscale structures: stabilizer-free nanodispersions, *Langmuir* 39 (4) (2023) 1515–1528, <https://doi.org/10.1021/acs.langmuir.2c02911>.
- [114] L.O. Kononov, Chemical reactivity and solution structure: on the way to a paradigm shift?, *RSC Adv.* 5 (58) (2015) 46718–46734, <https://doi.org/10.1039/C4RA17257D>.